Nano Energy 88 (2021) 106233

Contents lists available at ScienceDirect

Nano Energy

journal homepage: www.elsevier.com/locate/nanoen

In situ formed robust submicron-sized nanocrystalline aggregates enable highly-reversible potassium ion storage

Kuan-Ting Chen [a], Yi-Chun Yang [a], Lian-Ming Lyu [b], Ming-Yen Lu [b], Hsing-Yu Tuan [a,*]

[a] Department of Chemical Engineering, National Tsing Hua University, Hsinchu 30013, Taiwan
[b] Department of Materials Science and Engineering, National Tsing Hua University, Hsinchu 30013, Taiwan

ARTICLE INFO

Keywords:
Potassium-ion batteries
Anode
Nanocrystalline
Bismuth
Antimony
Ball milling

ABSTRACT

We report an electrode architecture made of submicron-sized nanocrystalline aggregates obtained *in situ* from ball-milled BiSb crystals during the potassiation/depotassiation process for use as a potassium ion battery electrode with high electrochemical performance and great stability. Nanocrystalline aggregates are individual particles composed of nanocrystals clustered together. The interconnected nanoparticle network as a potassium ion battery (PIB) electrode shows various advantageous characteristics, including adaption to related structures variation, stable SEI layer formation between the interface of electrode and electrolyte, and high efficiency in conductivity and ion migration/diffusion. As the anode of a PIB, the BiSb nanocrystalline aggregate achieves a high capacity of 514.1 mA h g^{-1} after 100 cycles at 0.25 A g^{-1}, a high-rate capability of up to 10 A g^{-1}, and an ultra-stable life cycle for 6000 cycles. A series of analyses including consecutive *in situ* X-ray diffraction measurements, *in situ* electrochemical impedance spectroscopy, and *ex situ* electron microscopy, are conducted to demonstrate the relevant reaction mechanism of the nanocrystalline aggregates during the evolution of composition as well as their structure during the cycling process.

1. Introduction

Due to the rarity of lithium (0.0017 wt% in the earth's crust), it is doubtful that lithium-ion batteries (LIBs) will meet the enormous demand for applications such as electric vehicles and grid-scale storage [1–3]. Potassium-ion batteries (PIBs) may replace LIBs as energy storage systems due to multiple unique attributes, such as low cost, abundant resource availability (approximately 2.09 wt%, ranking seventh in the crust), and low reduction potential [K^+/K (−2.94 V *versus* a standard hydrogen electrode); Li^+/Li (−3.04 V); Na^+/Na (−2.71 V)] [4–7]. The Stokes radius (3.6 Å) of K^+ in propylene carbonate (PC) solvent is the smallest when compared with those of Li^+ (4.8 Å) and Na^+ (4.6 Å), indicating its high ion mobility and ion conductivity [8–10]. Molecular dynamics simulation (MDS) studies demonstrate that the diffusion coefficient of K^+ is approximately three times that of Li^+ [11]. Based on these advantages, the replacement of Li^+ with K^+ may increase the rate capability of the battery without sacrificing energy density. However, the large ion radius of K^+ causes slow kinetics in the alloying/dealloying reaction and the relatively low potential of the K^+/K redox couple leads to increased side reactions as the solvent in the electrolyte is likely to be reduced on the electrode surface [12,13]. Therefore, it is important to explore the structure and electrochemical properties of PIB-based anode materials and further design electrochemically active electrodes with robust architecture.

Group 15 elements (such as Bi, Sb, and P) demonstrate high specific capacities for PIB anodes through alloy reactions with K^+ at low potentials (~ 0.1– 0.8 V *versus* K^+/K) [14–17]. For example, Sb has a high theoretical capacity of 660 mA h g^{-1} in a three-electron alloy reaction, where one Sb atom receives three K ions. However, the volume change of Sb during the potassiation/depotassiation process is as high as 407%, which leads to bulk Sb pulverization and results in rapid capacity decay [12,18]. Recently, bimetallic alloys have improved the performance of the Sb electrode. For example, an alloy of BiSb demonstrates promising results as the anode in sodium-ion batteries or PIBs [12,19,20]. A solid solution is formed by BiSb (Bi_xSb_{1-x}) at any molar ratio owing to its complete solid miscibility [12,18]. In addition, Bi stores K ions with a theoretical capacity of 385 mA h g^{-1}, achieving the theoretical capacity of Bi_xSb_{1-x} in the range of 385–660 mA h g^{-1} [16]. Moreover, the physical and chemical properties of Bi and Sb are highly similar on the electrochemical reaction platform. When BiSb reacts with K^+ *via* an alloying reaction, its intermediate state is the homogeneous ternary K_xBiSb that has a lattice softening effect, reducing the associated stress

* Corresponding author.
E-mail address: hytuan@che.nthu.edu.tw (H.-Y. Tuan).

https://doi.org/10.1016/j.nanoen.2021.106233
Received 3 May 2021; Received in revised form 1 June 2021; Accepted 5 June 2021
Available online 8 June 2021

during the potassiation/depotassiation process [12,18,21,22].

Recent studies test structural and material designs to enhance the stability of alloy- or conversion-type electrodes during the cycling process [23]. First, very fine nanoparticles (<5 nm) are synthesized to buffer the effect of volume changes and shorten the K^+ diffusion length [18,24]. However, nanomaterials as active materials tend to aggregate, and particle powdering may cause retarded kinetics due to the loss of nanoscale diffusion distance and electrical contact. Additionally, due to the freshly exposed surface of the active material, a thick mesophase SEI layer that significantly hinders charge transfer and causes rapid capacity decay forms continuously and uncontrolledly [25,26]. Therefore, various conductive carbon body/active materials (*e.g.*, electrospinning, porous carbon and other forms of carbon-based composites) are fabricated to serve as anode materials composed of small Sb-containing porous structures or nanocomposites to provide good conductivity and effectively buffer the large expansion of Sb. However, these methods require sophisticated high-temperature steps to obtain composite materials that still have excessive carbon content.

The alloy-based negative materials have higher potassium ion storage owing to alloying/dealloying reactions based on the transfer of multiple electrons per formula unit. Future development should focus on the design of stable nanostructured anode materials to maintain highly reactive K^+ alloying reaction, and improve cycle life and rate performance. The new design should be able to withstand large volume changes, buffer volume changes, or be assembled into a 3D structure to shorten the K^+ diffusion path, increase the electrode/electrolyte interface area, and promote the K^+ reaction with the anode. The preparation method should be simple and feasible with obvious improved effect, so that further practical application can be carried out. This paper reports the structure of submicron-sized BiSb nanocrystalline aggregates derived *in situ* from ball-milled BiSb crystals during the potassiation/depotassiation process. As presented in Scheme 1, the interconnected nanoparticle structure effectively reduces stress and the impact of severe volume changes. It also provides efficient K^+ diffusion pathways, better electron transmission, and stable SEI formation. The BiSb nanocrystalline aggregate as a potassium ion battery anode has a capacity of 514.1 mA h g^{-1} after 100 cycles at 0.25 A g^{-1}, a fast charge and discharge capability of up to 10 A g^{-1}, and an ultra-long cycling stability of up to 6000 cycles at 0.5 A g^{-1}. Therefore, the combination of nanocrystals and robust porous BiSb aggregates provides a promising strategy for constructing advanced electrodes for PIBs. The aggregates also become an effective conductive network with stable Bi/Sb composition control that inhibits the aggregation and volume expansion of BiSb nanocrystals during the cycling process.

2. Experimental section

2.1. Materials

Bismuth powder (99.5%, 325 mesh) and antimony powder (99.5%, 200 mesh) were purchased from Alfa Aesar. Potassium metal (98%), 1,2-dimethoxyethane (DME, anhydrous 99.5%), sodium carboxymethyl cellulose (NaCMC, average MW ~700,000) were purchased from Sigma-Aldrich. Potassium bis(fluorosulfonyl)imide (KFSI, 97%) was purchased from Chemical Block. The glass fiber was purchased from Advantec. Super-P and coin-type cells CR2032 were purchased from Shining Energy.

2.2. Material preparation

BiSb and BiSb/carbon nanotube (CNT) composites were synthesized *via* a facile high energy mechanical milling (HEMM) method using a planetary ball mill (PM 100, RETSCH). The raw materials of Bi powder and Sb powder (in a mole ratio of 1:1) were placed into a stainless-steel jar (12 cm^3) with stainless-steel balls (diameter of 3/8 in) at a ball-to-powder ratio of 100 (in weight) and sealed inside an argon-filled glovebox. The HEMM was conducted at room temperature with a rotation speed of 500 rpm for 12 h. The BiSb/CNT composite was also synthesized under the same conditions with the weight ratio of BiSb:CNT = 2:1.

2.3. Material characterizations

The phase of the as-prepared powders was characterized by x-ray diffraction (XRD, Bruker, D8 ADVANCE) with Cu-Kα radiation. The valence state and chemical composition of the samples were identified by a high-resolution x-ray photoelectron spectrometer (ULVAC-pH PHI QuanteraII). Their morphology and microstructure were observed *via* scanning electron microscopy (SEM, HITACHI-SU8010) with energy-dispersive X-ray spectroscopy (HORIBA, EX-250) and spherical aberration corrected scanning transmission electron microscopy (TEM, JEOL, ARM200F). For the SEM and TEM characterization of the cycled electrodes, the selected electrodes at different states were first washed whit DME to remove any residual salts. Thermogravimetric analysis (TGA) was conducted in N_2 using a thermogravimetric analyzer (TA, Q50) from 50 °C to 800 °C with a heating rate of 10 °C min^{-1}.

2.4. Electrochemical measurements

The working electrode was prepared by mixing 60% active material, 20% Super-P, and 20% CMC binder by weight in deionized water to form a slurry coated on copper foil, followed by vacuum-drying. The average mass loading of the active material was 0.6 ± 0.2 mg cm^{-2}. For

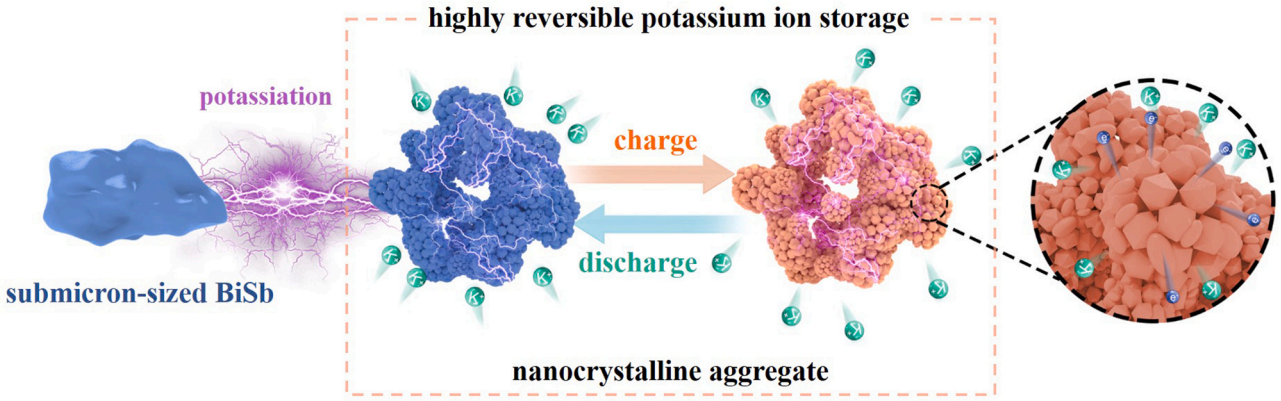

Scheme 1. Schematic illustration of submicron-sized BiSb to a nanocrystalline aggregate structure during the alloying and dealloying processes.

electrochemical measurements, the CR2032 type coin cell was assembled inside an argon-filled glove box. For the PIB cell (the working electrode in the investigated sample), potassium metal foil was utilized as the counter/reference electrode, glass fiber used as a separator and a mixture of 4.0 mol L^{-1} solution of KFSI salt in DME solvent applied as electrolyte for general use. The cells were cycled at 50 mA g^{-1} for a few times before the stability tests at 250 and 500 mA g^{-1}. The galvanostatic charge/discharge tests were conducted within the voltage range of 0.05–2.0 V. Cyclic voltammetry (CV) tests and electrochemical impedance spectroscopy (EIS) tests were conducted on a Biologic VMP3 electrochemistry workstation. The operando XRD patterns of BiSb were collected on a Bruker D8 ADVANCE diffractometer (Cu-Kα) for thirty cycles. The investigated sample as the working electrode, potassium metal foil as the counter electrode and reference electrode, and the 4 M KFSI in DME solution as the electrolyte. A current density of 50 mA g^{-1} was chosen for the charging and discharging processes between 0.05 and 2.0 V (*versus* K^+/K).

3. Results and discussion

Submicron-sized BiSb alloys were obtained by mechanically alloying Bi powder and Sb powder (1:1 wt ratio) at 500 rpm for 12 h. The XRD pattern of BiSb presented in Fig. 1(a) is consistent with the Rietveld refined results and corresponds to the rhombic facet of the *R*-3*m* (166) space group. The lattice parameters were calculated using the TOPAS V6 software by the crystal structure parameters listed in Table S1, according to the fitted curve. The position of the diffraction peak of BiSb is slightly lower than the standard peak position that corresponds to the Sb powder in the database (PDF#851324) as the larger Bi atom replaces the smaller Sb atom [20]. Except for the index, no other peaks were observed in the

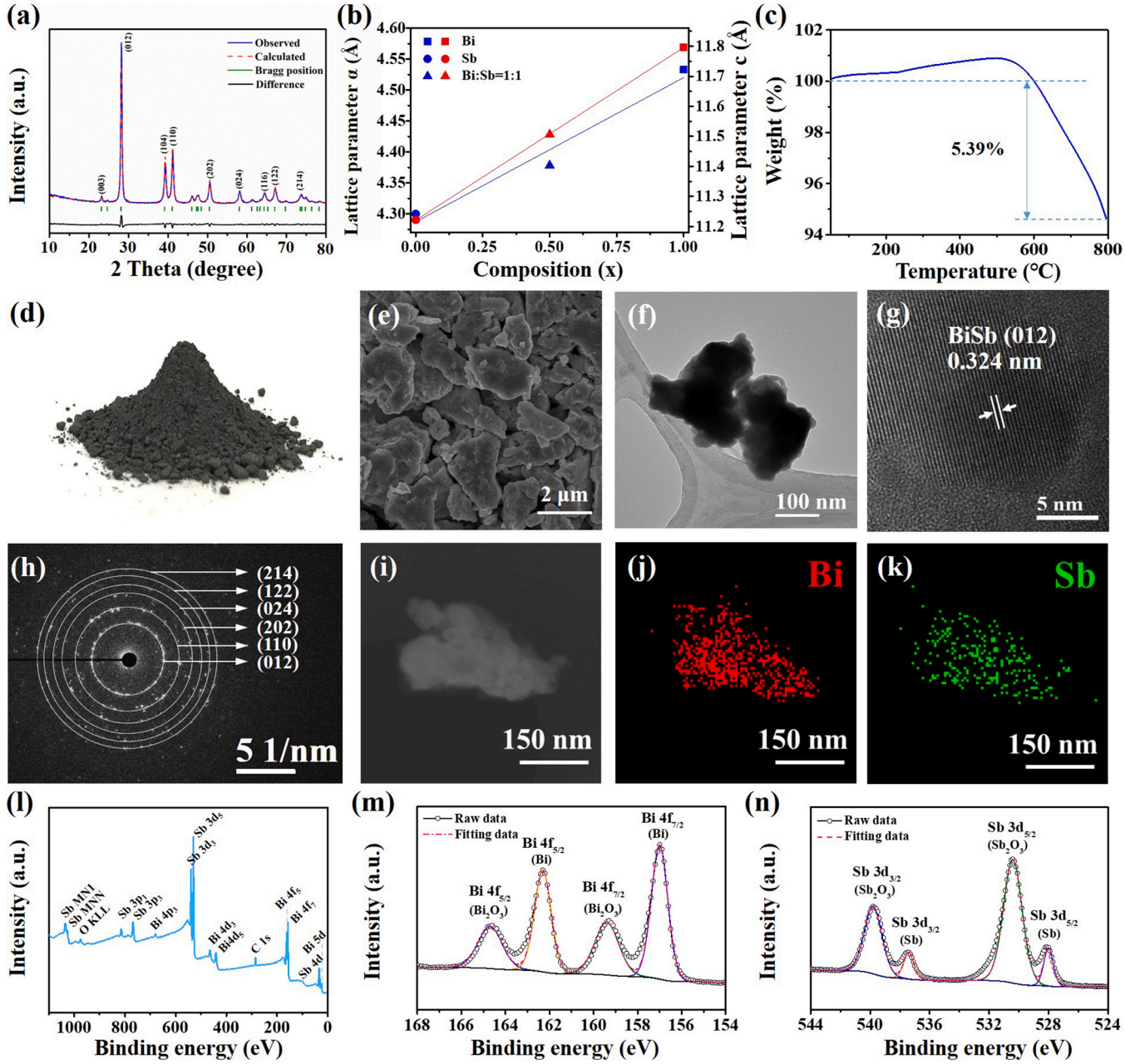

Fig. 1. (a) Rietveld refinement of the XRD pattern. (b) Dependence of the lattice parameters a (blue) and c (red) on the x of the BiSb. (c) TGA profiles of submicron-sized BiSb. (d) Photograph of BiSb powders. (e) SEM, (f) TEM, (g) HRTEM images and (h) SAED pattern of BiSb. (i–k) EDS mapping images of Bi and Sb. High-resolution XPS spectra of (l) survey XPS spectrum, (m) Bi 4f, and (n) Sb 3d for BiSb.

BiSb crystals. The calculated lattice parameter of BiSb (a = b = 4.38 Å and c = 11.51 Å) is almost identical to the theoretical value of BiSb fitting Vegard's law [27], demonstrating that Bi−Sb is homogeneously distributed with the atomic ratio = 1:1 in the alloyed nanocrystals (Fig. 1b). To evaluate the composition content of the BiSb composite material, TGA was conducted (Fig. 1c). From room temperature to 600 °C, the weight increase is attributed to the oxidation of BiSb. From 600 °C to 800 °C, the small weight loss is attributed to the evaporation of absorbed water [28]. As presented in Fig. 1(d), the color of the ball-milled BiSb powder is dark gray. The morphology and microstructure of the BiSb alloy observed *via* SEM and TEM (Fig. 1e and f) show irregularly shaped particles, ranging in size from submicron meters to a few microns. The high-resolution TEM (HRTEM) image (Fig. 1g) clearly demonstrates that the interplanar spacing is ≈ 0.324 nm, which corresponds to the lattice fringes on the (012) crystal plane of BiSb. The crystal structure of the BiSb particle in the TEM image was further confirmed by the diffraction ring in the selected area electron diffraction (SAED) mode (Fig. 1h), and consists of six diffraction rings indexed to the (012), (110), (202), (024), (122), and (214) planes of BiSb. Moreover, the corresponding energy dispersive spectroscopy (EDS) mapping images show a uniform distribution of the Bi and Sb elements with an atomic ratio of nearly1:1 (Fig. 1i–k). Fig. 1(l) presents the survey X-ray photoelectron spectroscopy (XPS) spectrum of BiSb powder. Fig. 1(m) demonstrates that the 4f core splits into Bi $4f_{5/2}$ (162.3 eV) and Bi $4f_{7/2}$ (157 eV) peaks, and the peak spacing is 5.3 eV [29,30]. Additionally, Bi_2O_3 $4f_{7/2}$ (159.4 eV) and Bi_2O_3 $4f_{5/2}$ (164.7 eV) are generated by forming oxides [31]. The peaks at 537.4 and 528 eV are caused by Sb $3d_{3/2}$ and Sb $3d_{5/2}$ (Fig. 1n) [32]. This confirms that oxides (Bi_xO_y and Sb_xO_y) are formed on the surface of the BiSb composite [12,33]. However, no oxide was detected by the XRD measurement, indicating that both the oxide signals were only amorphous surface oxides.

Fig. 2 presents the electrochemical properties of the BiSb alloy in half coin-typed cells using potassium as the counter electrode by the constant current method. Fig. 2(a) demonstrates the CV curve profile of the BiSb alloy at a scan rate of 0.1 mV s^{-1} in a voltage window of 0.0–2.0 V *versus* (K^+/K) for the first six cycles. A broad curve from 0.30 to 0.00 V in the initial cathodic process is observed and attributed to the potassiation of BiSb, decomposition of the electrolyte, or formation of a SEI layer on the electrode surface. The irreversible cathodic peak close to 0.0 V is attributed to the reaction of the oxides (Bi_xO_y and Sb_xO_y) on the BiSb alloy surface [12]. In the second to sixth scan, the two cathode peaks appeared at 0.48 and 0.00 V, respectively, indicating that K(Bi, Sb) and K_3(Bi, Sb) were formed by the K_x(Bi, Sb) alloy reaction. In the anodic scan, the two peaks at 0.75 V and 1.26 V correspond to the depotassiation reaction of K_3(Bi, Sb)→K(Bi, Sb)→(Bi, Sb) [12,21]. The CV curves obtained after the fourth scan nearly overlap, indicating that the potassiation/depotassiation reactions are highly reversible. In addition, in the homogeneous differential capacity (dQ/dV) graph of the BiSb

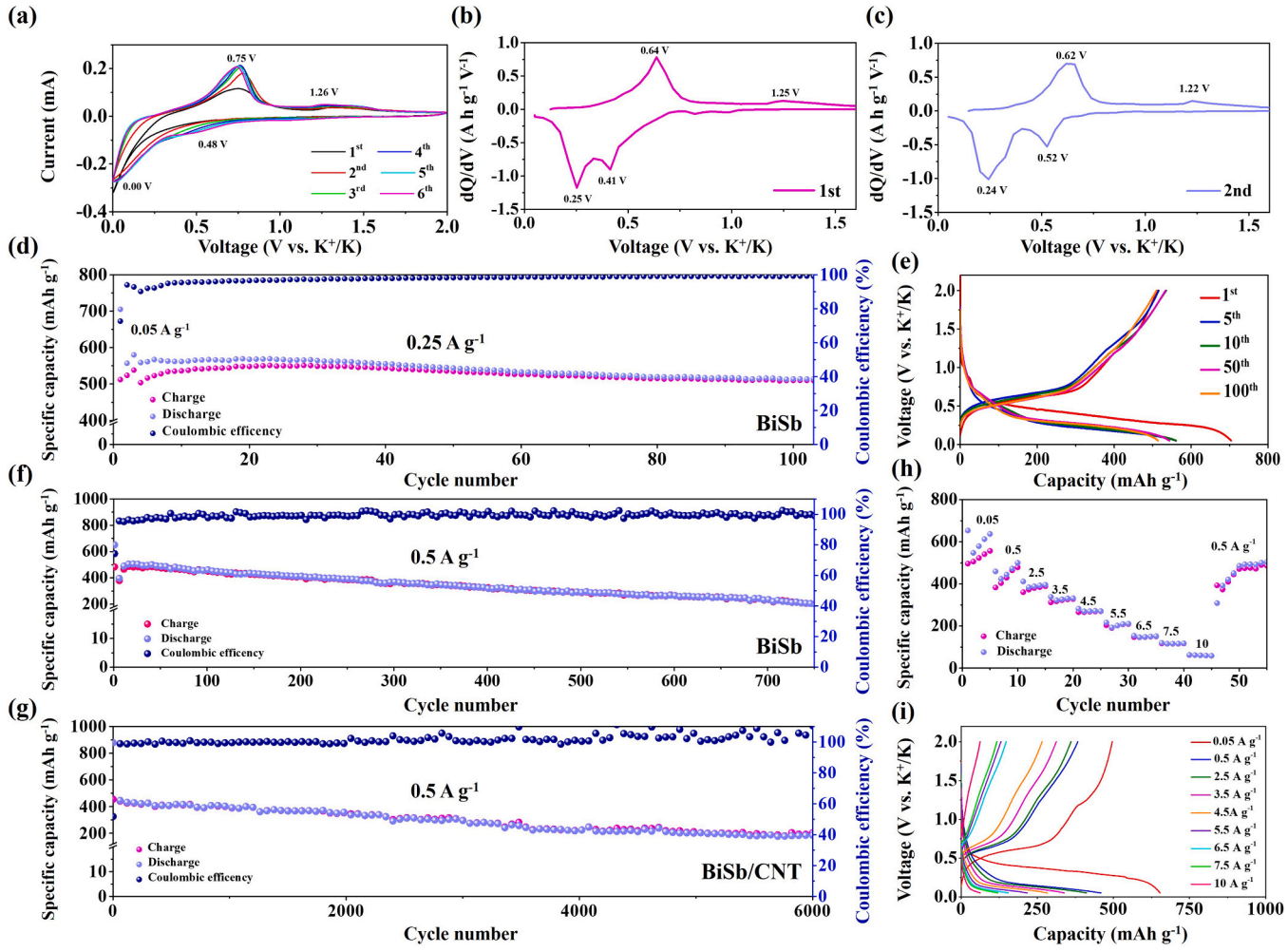

Fig. 2. Electrochemical characteristics of the BiSb and BiSb/CNT electrodes for PIB anodes. (a) CV curves of the BiSb electrode at a scan rate of 0.1 mV s^{-1}, differential capacity plots obtained for the (b) first and (c) second cycles, (d) cycling performance at 0.25 A g^{-1}, (e) corresponding charge/discharge curves for different selected cycles, and (f) cycling performance at 0.5 A g^{-1}. (g) Long-term cycling performance of the BiSb/CNT electrode at a current density of 0.5 A g^{-1}. (h) Rate capabilities of the BiSb electrode at various current densities and the (i) corresponding charge/discharge curves.

alloy (Fig. 2b and c), the two clear peaks at 0.25 and 0.41 V during the first discharge and at 0.24 and 0.52 V during the second discharge indicate the existence of a two-step reduction process during the potassiation reactions of Bi and Sb: (Bi, Sb)→K(Bi, Sb)→K_3(Bi, Sb). The two oxidation peaks at 0.64 and 1.25 V for the first cycle and 0.62 V and 1.22 V for the second cycle correspond to the two-step depotassiation reaction: K_3(Bi, Sb)→K(Bi, Sb)→(Bi, Sb) [18,20].

The first charge and discharge capacity at a current density of 0.05 A g^{-1} are 512.2 and 705.1 mA h g^{-1} (Fig. 2d), respectively, with an initial Coulombic efficiency of 72.6%. The capacity loss in the first few cycles may be due to the activation process (*i.e.*, the formation of the SEI layer or the irreversible reaction between K and the BiSb surface), leading to the improved K^+ accessibility between the BiSb surface and K^+. The BiSb electrode has a capacity of 514.1 mA h g^{-1} after 100 cycles at 0.25 A g^{-1}. Fig. 2(e) presents the corresponding constant current galvanostatic profiles of Fig. 2(d) and demonstrates highly overlapping curves and similar electrochemical reaction platforms from 1st to 100th cycle. This indicates stable alloying reactions that correspond to the gradual potassiation/depotassiation reactions during the discharging process and charging process, respectively. The cycling stability of the BiSb anode was further tested at a relatively high current density of 0.5 A g^{-1}. As presented in Fig. 2(f), the electrode delivers a reversible specific capacity of 236 mA h g^{-1} after 700 cycles, with an average Coulombic efficiency of 99.17%. This result indicates that after the initial activation process, the electrode/electrolyte interface quickly stabilizes for further potassiation/depotassiation reactions, and this is attributed to the structural stability of the BiSb electrode. To further improve the cycle stability of the BiSb alloy, the BiSb crystals were ball-milled with CNTs. The morphology and crystallinity of BiSb/CNT electrode are presented in Fig. S1. Fig. 2(g) presents the specific capacity of the BiSb/CNT electrode, exhibiting a capacity of 184 mA h g^{-1} even after 6000 cycles at 0.5 A g^{-1}, with each cycle's average Coulombic efficiency is almost 100%. The ultra-stable potassium ion storage is attributed to the beneficial effects of the conductivity improvement of the submicron-sized BiSb. The rate performance of the BiSb electrode was also investigated at various current densities of up to 10 A g^{-1} (as presented in Fig. 2h), displaying 653.3, 459.1, 411.3, 338.5, 282.1, 216.5, 153.8, 120.1, and 62.9 mA h g^{-1} at the current densities of 0.05, 0.5, 2.5, 3.5, 4.5, 5.5, 6.5, 7.5, and 10 A g^{-1}, respectively. These results suggest that the electrode has an excellent rate performance at high charge/discharge current densities. After the current density returned to 0.5 A g^{-1}, the specific capacity remained at approximately 492.3 mA h g^{-1}. Compared with the value before the high-rate cycling process, this was only a loss of 1.54%. As the current density increases, the shape of the charge/discharge curve is well maintained, further confirming its highly reversible reactions and low overpotential at high

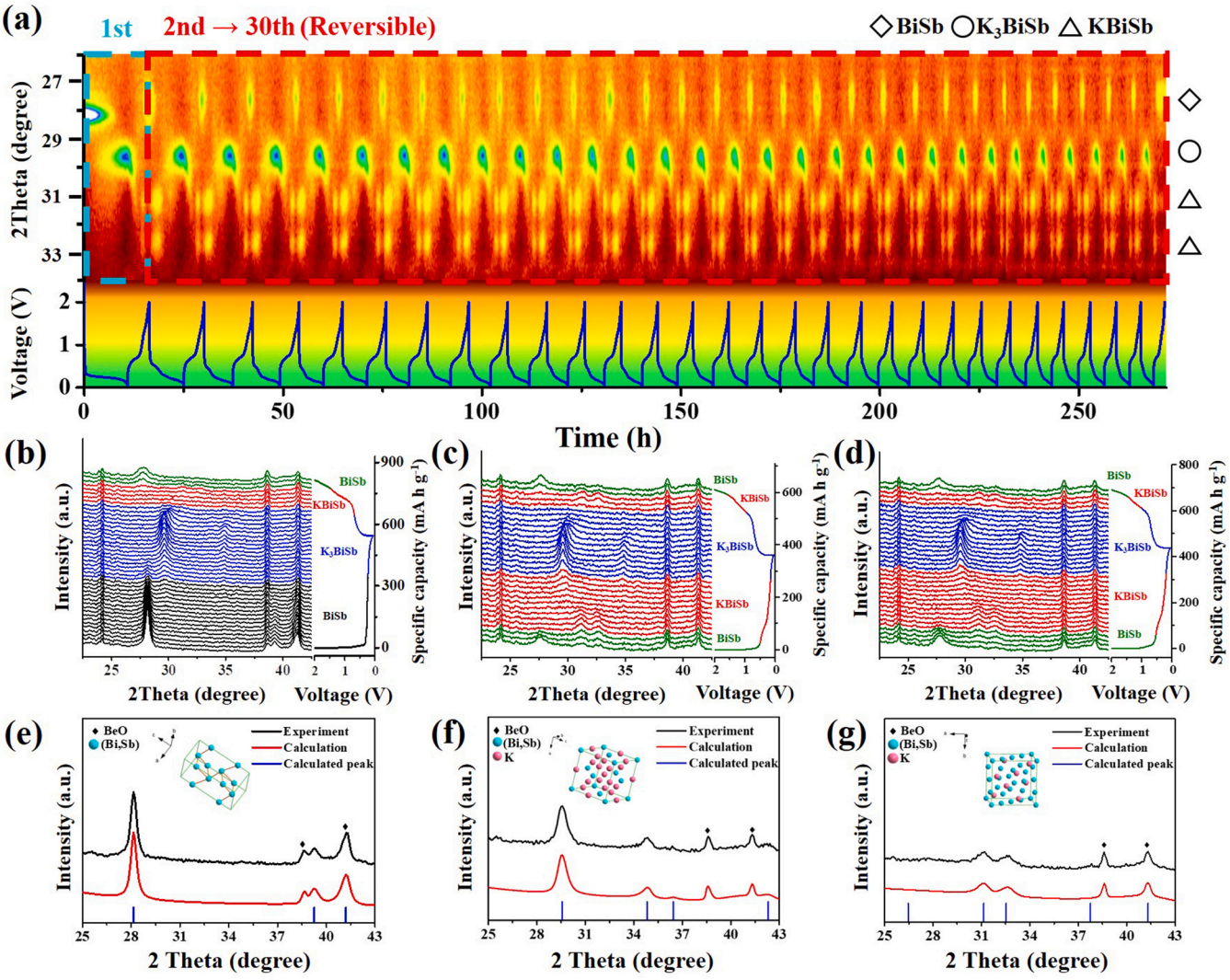

Fig. 3. (a) *In situ* contour plot of the operando XRD results obtained for the 30th cycle potassiation/depotassiation process of the BiSb electrode. (b–d) Line plots of the *in situ* XRD results. (e–g) Experimental and calculation results of XRD patterns and corresponding atomic structures (e) (Bi, Sb), (f)K_3(Bi, Sb), and (g) K(Bi, Sb).

charge/discharge rates (Fig. 2i).

The crystal structure of the electrode material is closely related to the performance of the battery, including power and energy density, cycle life, and rate capability. A deep understanding of these relationships is of great significance for the optimization of the current electrode systems and development of new electrode materials with better electrochemical performance. Studies show that *in situ* XRD measurement is a very powerful technique that provides information on the crystal structure and phase transition of the crystal electrode material during cycling. Fig. 3(a)–(d) demonstrate *in situ* contour mapping and XRD line plots to observe the structural transition and phase evolution of a BiSb electrode. *In situ* XRD was conducted during the electrochemical cycle of 0.05 A g^{-1} at 0.05–2.0 V. The experimental results and subsequent calculations of the (Bi, Sb), K(Bi, Sb), and K_3(Bi, Sb) phases are compared in Fig. 3(e)–(g). In the first charge and discharge cycle, at approximately 0.23 V, a peak of about 29.67° was observed, corresponding to the (220) plane of K_3BiSb (PDF#00-019-0935). This indicates that BiSb potassium was converted to K_3BiSb. Then, during the charging process, new peaks at 31.12° and 32.65° was observed near 0.70 V, referring to KBiSb (PDF#04-010-8776) on the (311) and (222) planes, respectively. This indicates that K_3BiSb was depotassiated into KBiSb. With the continuous depotassiation process, a BiSb peak of 27.71° was observed near 1.5 V, indicating that KBiSb returned to BiSb. In the second cycle, peaks at 31.2° and 32.65° were observed around 0.48 V, corresponding to the (311) and (222) planes of KBiSb. This was different from the first cycle, showing that KBiSb was first formed by potassiation of BiSb. At about 0.15 V, a peak of 29.59° appeared, corresponding to the (220) plane of K_3BiSb. This indicates that KBiSb transformed into K_3BiSb. Then, during the charging process, peaks close to 31.2° and 32.65° appeared near 0.95 V, corresponding to KBiSb, indicating that K_3BiSb was depotassiated to KBiSb. With the continuous depotassiation process, a BiSb peak of 27.63° appeared near 1.56 V, indicating that KBiSb returned to BiSb. The TEM images after the first discharge state further verify the structural evolution of BiSb. Fig. 4 demonstrates that the BiSb alloy changed from a bulk material to a K_3BiSb nanocrystalline aggregate composed of several uniform nanoparticles in the potassiation process. It is uniformly distributed with small nanocrystals in which each particle is gathered, and the shape of the particles is irregular. Additionally, these primary particles tend to be arranged randomly, resulting in multiple spatial voids/pores. This promotes greater electrolyte wetting and subsequently provides numerous electrochemically active sites during the reaction.

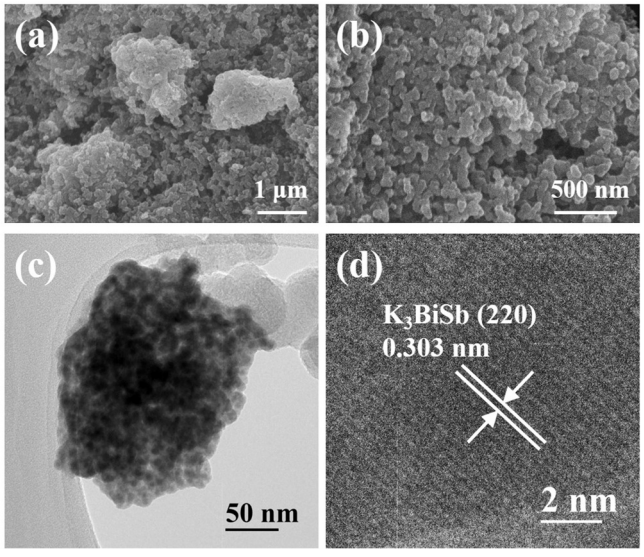

Fig. 4. (a, b) SEM, (c) TEM, and (d) HRTEM images of the BiSb electrodes in the initial discharge state.

To clearly understand the evolved structure and composition of BiSb after cycle process, the composition and morphology evolution of the BiSb anodes were investigated by consecutive *in situ* XRD and *ex situ* SEM and TEM at different cycles. From 5^{th} to 6000^{th} cycles, the structural changes of the BiSb alloy nanocrystals and the morphology and microstructure of the BiSb alloy were observed (Figs. 5 and 6). Fig. 5(a) presents the SEM image of the structure of the BiSb alloy after the fifth cycle with uniformly distributed spherical particles. The morphology of the BiSb aggregate is similar to that of the initially potassiated BiSb, and the internal particles of the aggregate are compactly connected to each other. In Fig. 5(a), the electrode surface after the 5^{th} cycle is uniformly covered by a SEI layer. In addition, as presented in Fig. 5(b)–(e), the nanocrystalline aggregate maintains a similar spherical shape in the anode material. The electrode morphology results of 320 cycles are similar to those of 10–30 cycles. To explore cycle stability of the BiSb electrode, the electrode using 4.0 M KFSI in DME as the electrolyte was investigated by TEM. It is clearly observed that a compact SEI layer evenly covers the electrode surface (Fig. S7). The BiSb electrodes was investigated by XPS analysis after 1, 5, 10, 15 cycles, as shown in Fig. S8, to understand the surface chemistry of the SEI layer. High-resolution S2p peak can split into two peaks after 1 cycle and four peaks after 15 cycles, located at 162.5, 165, 167, and 168.6 eV, which are assigned to the $K_2S_2O_3$, K_2SO_3, K_2SO_4, and $KHSO_4$, respectively (Fig. S8a) [34,35]. As shown in Fig. S8b, the C 1s spectra can be splitted into three peaks located at 284.4, 286.1, and 287.4 eV, which are assigned to C–C, C-O, and C═O species in the surface layer, respectively [36,37]. The O 1s spectra on BiSb electrolytes contain two peaks at 528.7 eV (C═O) and 530.4 eV (C–O) (Fig. S8c). The C–O and C═O species in the surface layer are originated from the decomposition and reduction of DME solvent [38]. The strong KF signal with a binding energy at 683 eV is observed due to the residual KFSI on the surface of the BiSb electrode (Fig. S8d) [39]. The XPS analysis indicated that the BiSb electrode surface with the electrolyte of 4 M KFSI in DME is mainly composed of inorganic salts. And the DME-based electrolyte is beneficial to improve electrode stability by constructing robust and ultra-thin SEI films [38]. Additionally, the Bi 4f and Sb 3d spectra disappear after 15 cycles due to the stable SEI layer formation on the BiSb electrode surface (Fig. S9).

This result shows a great reaction stability at the interface between BiSb electrode and electrolyte, forming a thin and stable SEI layer. The SEI layer is not only an insulator of electrons, but also a K^+ transport conductor. A stable SEI layer is essential to achieve a long cycle life, and an excessively thick or unstable SEI layer usually leads to electrolyte consumption, larger contact resistance, and a long distance between the current collector and the negative electrode material. The TEM image (Fig. 5f–j) shows that the BiSb nanocrystalline aggregates after the 5^{th}, 10^{th}, 15^{th}, 30^{th}, and 320^{th} cycle, respectively. The size of individual nanocrystalline aggregate is roughly hundreds of nanometers, and the grain size of each nanoparticle is about 3–10 nm: they are still tightly connected to form a uniformly distributed nanocrystal matrix. This result shows that the stress caused by the volume change did not cause the nanocrystalline aggregate to break after alloying and dealloying process. In addition, the interconnection of each nanocrystals and the lattice-softening effect in Bi-Sb alloy also enhance the structure integrity. The nanocrystals after cycling exhibit highly crystalline structure. The HRTEM images (Fig. 5e–o) of the five cycled BiSb clearly shows the clear lattice fringe with a lattice distance of 0.323 nm, corresponding to the (012) surface of the BiSb crystal phase. In the sample from 4775^{th} cycle (Fig. 6a), the SEM image demonstrates a uniform coating of the SEI layer on each nanocrystalline aggregate. The TEM image (Fig. 6b and c) demonstrates that the structure of the nanocrystalline aggregate is similar to that of the one from 320^{th} cycle, and the morphology only slightly changes. The size of the nanoparticle is also approximately 3–10 nm, and the crystal structure is perfectly preserved. Moreover, the disassembled electrode maintains a complete electrode surface, and no cracks or loose fine particles are observed on the electrode surface (inset of Fig. 6a). The unprecedented long cycle life is a comprehensive result

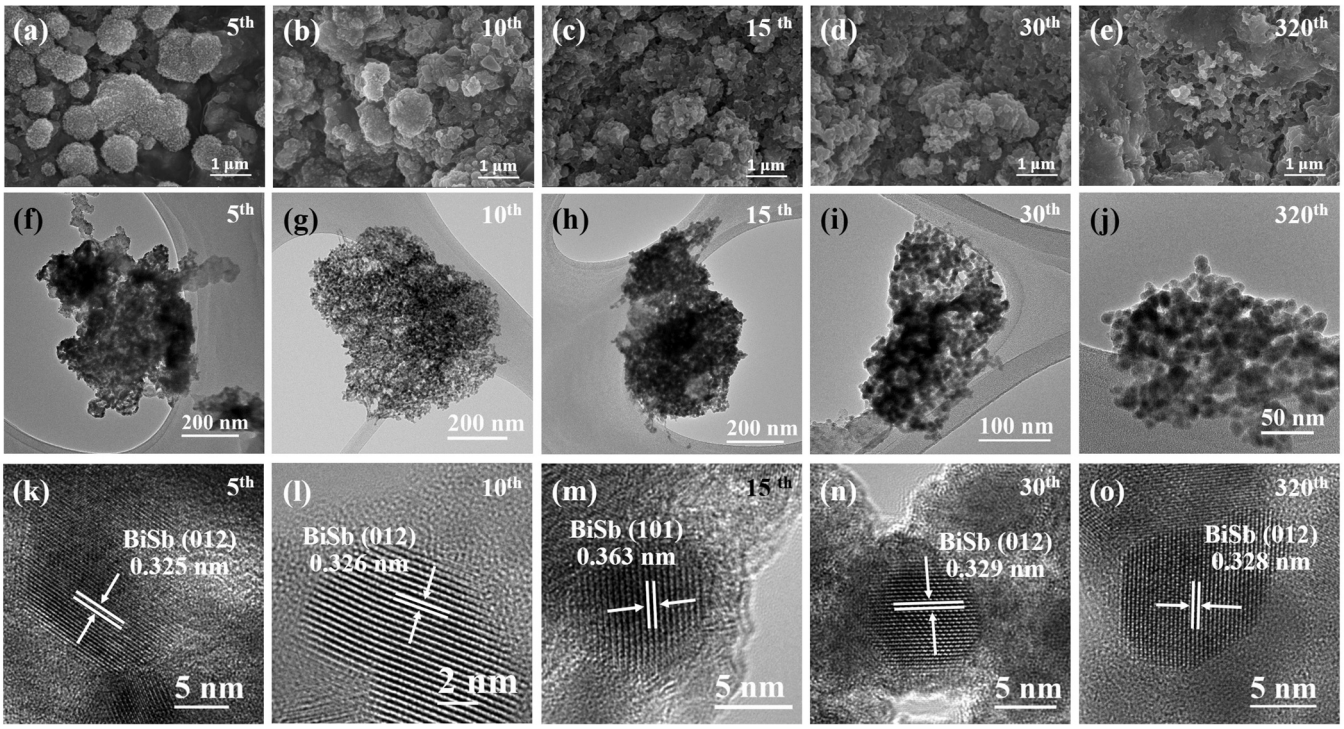

Fig. 5. SEM, TEM, and HRTEM images of the BiSb electrodes after 5, 10, 15, 30, and 320 cycles.

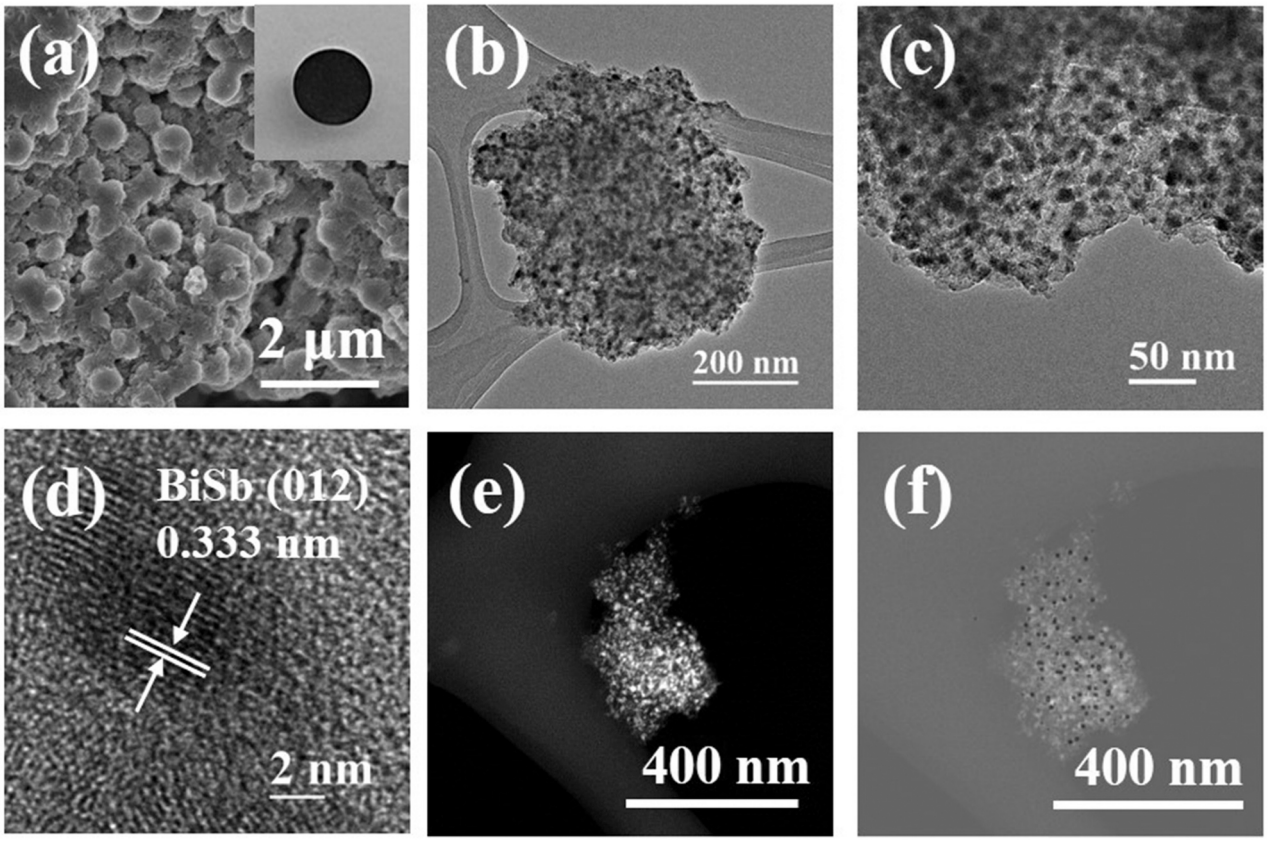

Fig. 6. (a) SEM, (b–c) TEM, (d) HRTEM images and (e, f) EDS mapping images of the BiSb/CNT electrode after the 4755th cycle. Red dots: Bi. Green dots: Sb. Inset: Digital photo of the BiSb/CNT electrode corresponding to (a).

of the stability of the nanoparticle aggregate structure. During the charging/discharging process, the nanoparticle size in the nanocrystalline aggregate hardly changes, indicating that the nanoparticle sufficientlybuffers the volume change. As the size is smaller than its critical diameter, the potassiation/depotassiation process does not lead to pulverization. The approximate void of each nanoparticle is maintained at several nanometers, and the void remains almost unchanged (in experimental uncertainty within range) after multiple consecutive cycles of potassiation/depotassiation. It is possible that the existence of this void also buffers the volume change effect. With constant nanoparticle spacing during the charge/discharge cycle, the electrode minimizes the influence of electrochemical reactions that may cause anode instability, and the network structure reduces strain and minimizes surface energy, thereby achieving longer cycle stability. In addition, EDS analysis was conducted on BiSb with a thin film structure composed of extended single-crystal domains. The results demonstrate that the uniform BiSb component distribution was maintained before the initial charge and discharge (Fig. 6e and f). The excellent performance of the BiSb electrode is caused by the unique structure of the nanocrystalline aggregates. The 30 consecutive cycles of the *in situ* XRD contour plot (Fig. 3a) only contained three main peak positions [BiSb (27.63°), K_3BiSb (29.59°), and KBiSb (31.2° and 32.65°)], and no significant peak displacement was observed. In addition, the change sequence of the peak position at each time is the same as the second charge/discharge cycle. This result suggests that the chemical reaction of the BiSb electrode remains unchanged and highly reversible during the consecutive cycle.

Moreover, Fig. 7 presents the TEM, the HRTEM images and the SAED patterns of the BiSb electrodes at different discharge/charge states in the 16th cycle. The BiSb nanocrystalline aggregates transformed to KBiSb and K_3BiSb at 0.4 V and 0.14 V at the discharge state, respectively. They were then transformed back to BiSb after charging to 2.0 V. The TEM demonstrated that the interior was still composed of multiple nanoparticles during the overall discharge/charge state. It should be noted that the architecture (the nanocrystal size and shape) of the nanocrystalline aggregate remained unchanged during the depotassiation process. The TEM investigation of the phase evolution is consistent with what was observed during *in situ* XRD studies. After combining with the observations of *in situ* XRD and TEM, it was determined that the entire structure maintained very stable characteristics in terms of composition and structure during the potassiation/depotassiation process. The overall process is summarized as follows:

st cycle

I: (Bi, Sb) + K^+ + e^- → K_3(Bi, Sb) (~0·23 V)

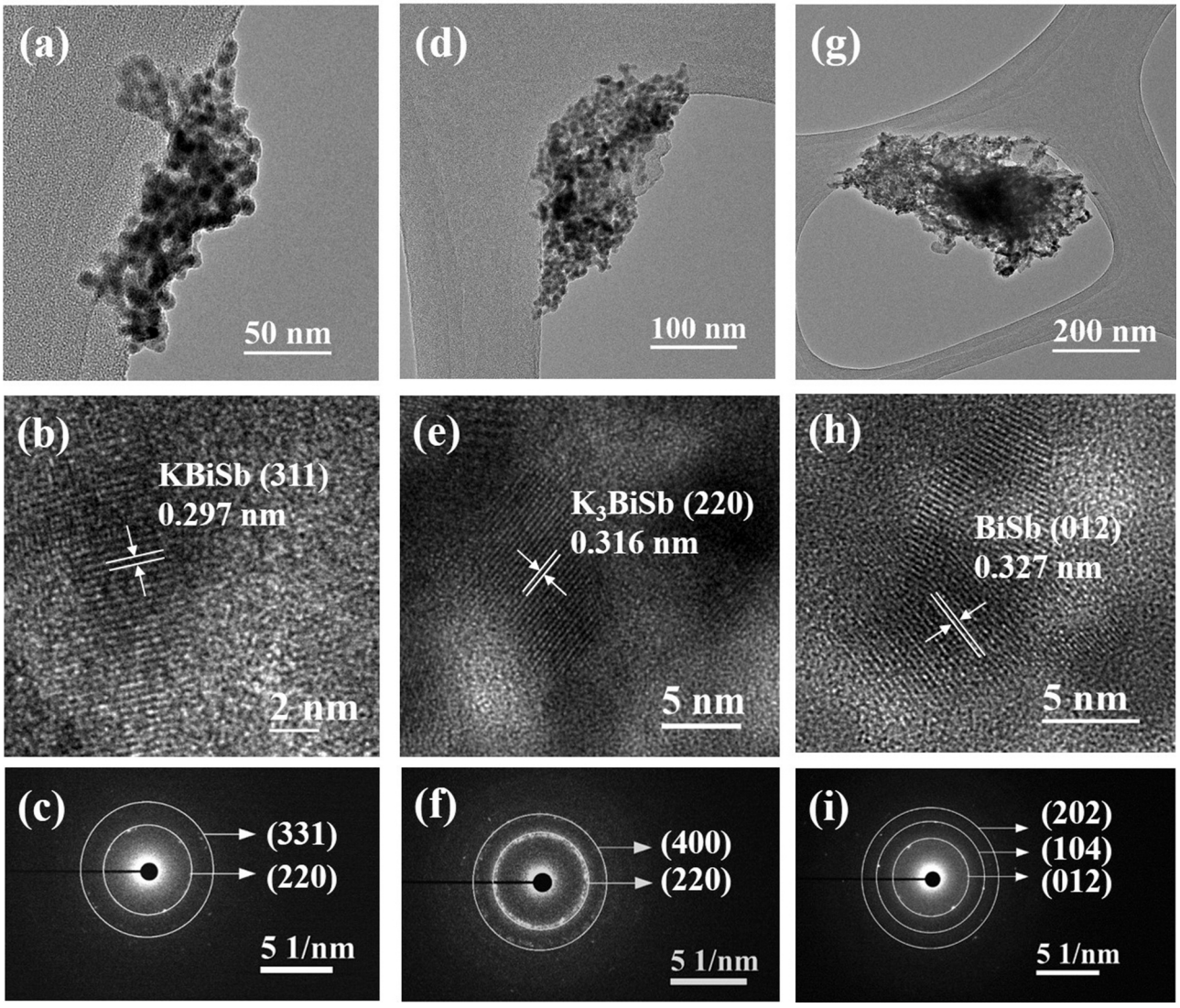

Fig. 7. TEM, HRTEM images and SAED patterns of the BiSb electrodes at different discharge/charge states in the 16th cycle. (a–c) After discharging to 0.4 V. (d–f) After discharging to 0.14 V. (g–i) After charging to 2.0 V.

submicron-sized crystals → nanocrystalline aggregate

II: $K_3(Bi, Sb) - K^+ - e^- \rightarrow K(Bi, Sb)$ (~0.70 V)

III: $K(Bi, Sb) - K^+ - e^- \rightarrow (Bi, Sb)$ (~1.50 V)

2nd cycle ~ 6000th cycle

I: $(Bi, Sb) + K^+ + e^- \rightarrow K(Bi, Sb)$ (~0.48 V)

II: $K(Bi, Sb) + K^+ + e^- \rightarrow K_3(Bi, Sb)$ (~0.15 V)

III: $K_3(Bi, Sb) - K^+ - e^- \rightarrow K(Bi, Sb)$ (~0.95 V)

IV: $K(Bi, Sb) - K^+ - e^- \rightarrow (Bi, Sb)$ (~1.56 V)

The electrochemical kinetic analysis of the BiSb alloy was systematically studied by CV. Fig. 8(a) presents the CV of the BiSb alloy at a scan rate ranging of 0.1–1.2 mV s^{-1} in the potential range of 0.05–2.0 V. The capacitance effect is determined from the curve, where the measured peak current (i) and scan rate (ν) follow a power law relationship: $i = a\nu^b$, where a and b are constants determined from the slope of the logarithmic i graph *versus* the logarithmic ν graph as presented in Fig. 8(b). The b value of 0.5 indicates the diffusion-controlled capacitive process, and b value of 1 indicates the surface-capacitance-based dominant process [40–43]. In this case, the b values of the cathode peak and anode peak are calculated to be 0.76 and 1.01, respectively. These values mainly indicate the surface-capacitance control process. The pseudocapacitance contribution rate at different scan rates is further quantified by the following formula, which was developed by Dunn et al.:

$$i\ (\mathrm{V}) = k_1\nu + k_2\nu^{1/2},$$

This equation can be rewritten as.

$$i(\mathrm{V})/\nu^{1/2} = k_1\nu^{1/2} + k_2$$

where $k_1\nu^{1/2}$ and $k_2\nu$ denote the contribution of the diffusion control process and the pseudocapacitance effect, respectively [44,45]. As presented in Fig. 8(c), the orange shaded area corresponds to the total capacitance current response at a scan rate of 0.4 mV s^{-1}, accounting for the pseudocapacitance fraction of ≈ 74%. At the lower scan rate of 0.1 mV s^{-1}, the capacitance contribution still reaches 76%. The fraction of the capacitance contribution at different scan rates is presented in Fig. 8(d). Fig. 8(e) shows the galvanostatic intermittent titration technique (GITT) curve of the BiSb electrode. According to Fick's second law and the below equation [46,47],

$$D_{K^+} = \frac{4}{\pi\tau}\left(\frac{m_B V_M}{M_B S}\right)^2\left(\frac{\Delta E_S}{\Delta E\tau}\right)^2 \left(\tau \ll \frac{L^2}{D}\right)$$

This formula calculates the potassium diffusion coefficient (D), where V_M denotes the molar volume of the active material; M_B, the molecular weight of the material; m_B, the mass of the active material in the electrode; S, the geometric area of the electrode; τ, the duration of the current impulse; t, the duration time of the current pulse, and L, equal to the thickness of the electrode. ΔE_s and ΔE_t are defined as shown in Fig. S10. It is found that the D_{K+} value of the BiSb alloy nanocrystals ranges from 5.79×10^{-10} to 1.87×10^{-11} cm^2 s^{-1} at potassiation voltages and 3.73×10^{-10} to 2.62×10^{-11} cm^2 s^{-1} at depotassiation voltages, respectively (Fig. 8f). This indicates that the BiSb alloy nanocrystals present a large diffusion coefficient due to a large number of spatial voids/pores.

Further analysis was conducted through *in situ* EIS kinetic measurements to explore the electrochemical kinetics of the structural evolution of BiSb during the charge/discharge process (Fig. 9). Fig. 9(a) and (b) present the Nyquist plots recorded during the *in situ* EIS analysis of the BiSb electrode in the initial cycle. As the electrode discharged from open-circuit voltage (OCV) to 1.25 V, the formation of the K^+ insertion and SEI layer slightly increases the resistance (Fig. 9a). When the voltage is discharged from 1.25 V to 0.05 V, BiSb is converted to K_3BiSb, and its structure gradually changes from bulk to ultra-fine nanocrystals, making the resistance significantly smaller. When the cell is gradually charged to 2.0 V, there is no significant change in resistance (Fig. 9b). Fig. 9(c) and (d) present the Nyquist plot of the *in situ* EIS analysis of BiSb in the 15th cycle and the electrochemical kinetics after the electrode stabilized. When discharged to 0.5 V, the resistance becomes significantly smaller. This is attributed to the formation of a stable SEI layer and the formation of ultra-fine nanocrystals. From 0.5–0.05 V, no significant change in resistance has been observed, and this is attributed to the stability of the K^+ embedding process (Fig. 9c). When further charged to 2.0 V, the resistance returns to the initial value, indicating high reversibility of the whole electrode (Fig. 9d).

Finally, a detailed electrochemical performance of the BiSb electrode and the Sb-based electrode material published recently is compared with this work. The radar chart in Fig. 10 shows the initial Coulombic efficiency (ICE), the specific capacity at a low rate (0.05–0.5 A g^{-1}) after 50 cycles (50th SCL), the cycle number, the highest rate capability (HR), and the specific capacity at high rate (1–2.5 A g^{-1}) (SCH). The performances of twelve Sb-based electrode materials were compared, including Sb-based carbon composite anodes (Sb@CNF [48], Sb@C PNFs [49], Sb/CNF-0.5 [32] and Sb@MCMB-3 [50]), and Sb compounds (BiSb@P [18], Se@Sb@C [51], Sn-Sb LSM [52], Sb_2Se_3@NC@rGO [53], Sb_2S_3-Bi_2S_3@C@rGO [54], BiSb@Bi_2O_3/SbO_x@C [28], Ti_3C_2-Sb_2S_3 [55], and Sb_2S_3-C@Nb_2O_5-CNFs [56]). As shown from the radar chart, by comparing these five indicators, this work covers the largest area, showing that the electrochemical performance of the potassium ion electrode is quite balanced. Although it ranked third in SCH (411 mA h g^{-1}) and third in ICE (72.65%), it demonstrated the best performance in terms of cycle number, HR, and 50th SCL. The BiSb anode film in this work is a submicron-sized spherical aggregate constructed from nanocrystals derived from submicron-sized crystals during the cycling process. It has a large specific surface area and can be effectively wet with the electrolyte with the optimized electrolyte contact. Owing to its porous nature, the nanocrystalline aggregate also enhances the surface adsorption of potassium ions. Small BiSb nanocrystals shorten the transfer length of K^+ and increase the surface area of the active material, both of which are beneficial to the K^+ potassiation/depotassiation reaction. Since the nanocrystals are in close contact with adjacent crystal grains, this symbiosis improves the transport of electrons through the crystal grain boundaries [57], shortens the diffusion length of potassium ions, and reduces the resistance of the electrode during cycling, allowing rapid passage of electrons and less recombination. The kinetic analysis of this structure reveals that the range of the surface pseudo-capacitance process is significantly expanded. This aggregate structure prevents the electrode from pulverization with enhanced electrochemical stability. As presented in Fig. 10, the cycle life of most Sb-based potassium ion batteries is shorter than 1000 cycles. This is because the volume of Sb sharply changes, making the electrode easy to pulverize, and a thick or uneven SEI film is formed due to a cracked or fragile structure. The robust nanocrystalline aggregates, (*i.e.*, submicron-sized spheres composed of extremely small nanocrystals) have a relatively high surface area, interconnected conductive crystal grains, and narrow pore size distribution to enable highly reversible potassium ion storage. Therefore, the BiSb nanocrystalline aggregates not only achieve a stability of up to 6000 cycles, but also have excellent performance in HR and 50th SCL. In addition, some research work on full cell for the practical application of Sb-based PIB in the future [12,58,59].

4. Conclusions

Submicron-sized nanocrystalline aggregates are derived *in situ* from submicron BiSb crystals during the potassium ion alloying/dealloying process and demonstrate excellent electrochemical performance as PIB anodes. Based on the analysis of the structure of the aggregates (*i.e.*, the morphology of the alloyed anodes observed in consecutive *in situ/ex situ* measurements), this kind of nanocrystal aggregate underwent a highly reversible reaction of BiSb↔KBiSb↔K_3BiSb throughout all thousands of cycles. Kinetic dynamic studies, including CV, GITT, and *in situ* EIS, show a high diffusion coefficient, enhanced electron transport due to the

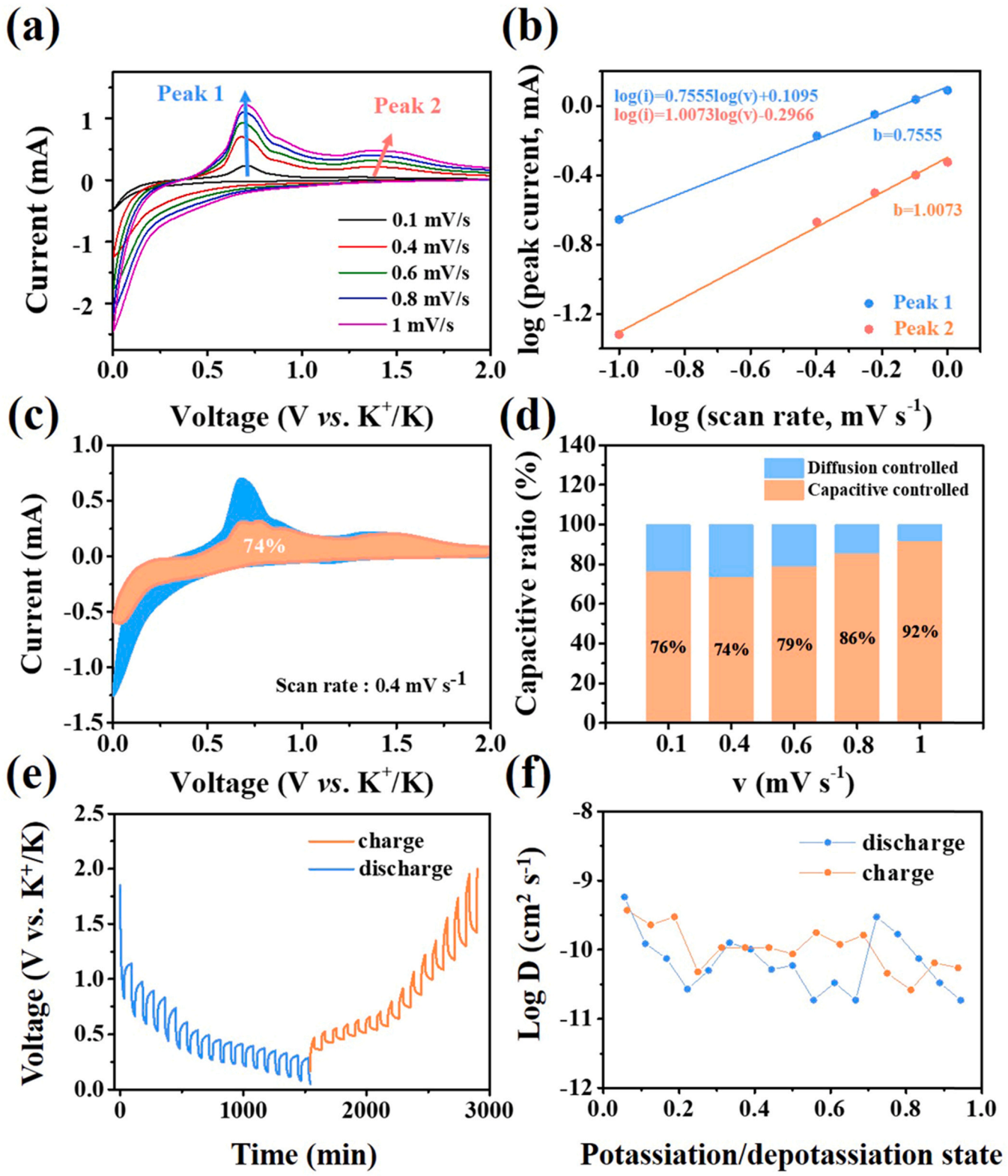

Fig. 8. Electrochemical kinetics analysis of the BiSb electrode. (a) CV curves at various scan rates in the range of 0.1–1.0 mV s^{-1}, (b) linear relation of log(i, peak current) and log(v, scan rate), (c) the CV profiles displaying the K-ion diffusion–controlled contribution at 0.4 mV s^{-1} and (d) the ratio of capacitive and diffusion-controlled contribution to K-ion storage *versus* scan rate. (e) GITT profiles of the first charge/discharge process at 0.1 A g^{-1} and (f) the calculated K-ion diffusion coefficient.

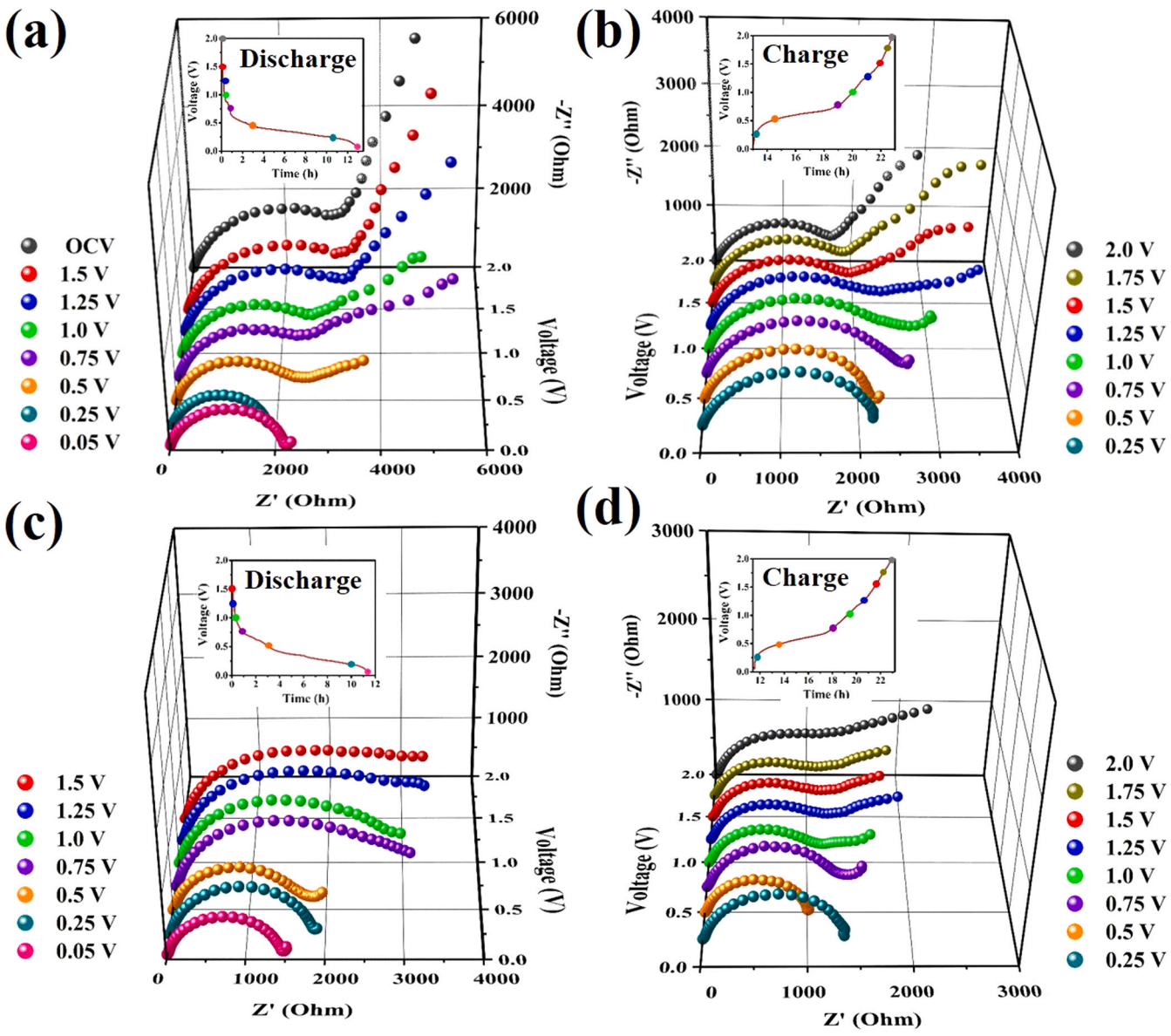

Fig. 9. *In situ* Nyquist plots of the BiSb electrode for the (a–b) 1st, (c–d)15th cycles at pre-selected potentials, inset: charge/discharge curves.

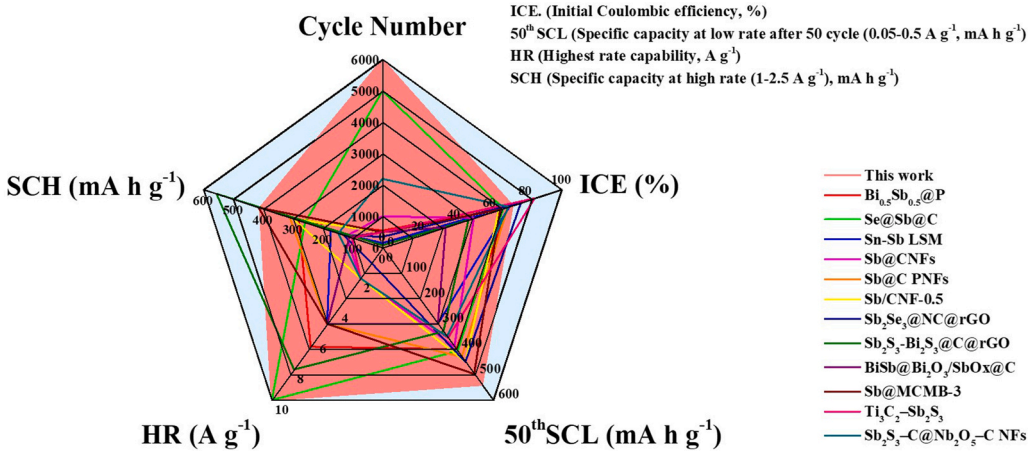

Fig. 10. Comparison results of the cycle number, initial Coulombic efficiency (ICE), specific capacity at low rate after 50 cycles (0.05–0.5 A g^{-1}) (50th SCL), highest rate capability (HR), and specific capacity at high rate (1–2.5 A g^{-1}) (SCH) between the BiSb electrode and other previously reported electrodes for PIBs.

retained highly specific surface area, and high structural maintenance for potassium ion adsorption and electrolyte diffusion. As a result, a nanocrystalline aggregate has multiple advantages: (1) The crystal domain of each single nanocrystal (3–10 nm) is small enough to relax the stress induced from the large volume change occurring during potassiation/depotassiation process, and to shorten the transfer length of K^+. (2) The interconnected nanocrystal aggregates improve the electron and ion transport through the crystal grain boundary. (3) The porous aggregate promotes the wettability of the electrolyte owing to their large internal effective surface area and provide robust architecture to significantly confirm the structural integrity and stability of the SEI layer covered on the electrodes.

CRediT authorship contribution statement

Kuan-Ting Chen: Conceptualization, Methodology, Data curation. **Yi-Chun Yang:** Investigation. **Lian-Ming Lyu:** Data curation. **Ming-Yen Lu:** Investigation. **Hsing-Yu Tuan:** Conceptualization, Resources, Supervision, Writing - review & editing.

Declaration of Competing Interest

The authors declare that they have no known competing financial interests or personal relationships that could have appeared to influence the work reported in this paper.

Acknowledgments

This work was supported by the financial support from the Young Scholar Fellowship Program by Ministry of Science and Technology, Taiwan (MOST 110-2628-E-007-001). H.-Y. Tuan also acknowledges the financial support of National Tsing Hua University, Taiwan through the grant of 109QI030E1.

Appendix A. Supporting information

Supplementary data associated with this article can be found in the online version at doi:10.1016/j.nanoen.2021.106233.

References

[1] P. Xiong, P. Bai, S. Tu, M. Cheng, J. Zhang, J. Sun, Y. Xu, Red phosphorus nanoparticle@3D interconnected carbon nanosheet framework composite for potassium-ion battery anodes, Small 14 (2018), 1802140.
[2] C. Li, A.T. Bi, H.L. Chen, Y.R. Pei, M. Zhao, C.C. Yang, Q. Jiang, Rational design of porous Sn nanospheres/N-doped carbon nanofibers as an ultra-stable potassium-ion battery anode material, J. Mater. Chem. A 9 (2021) 5740–5750.
[3] M. Zhou, P. Bai, X. Ji, J. Yang, C. Wang, Y. Xu, Electrolytes and interphases in potassium ion batteries, Adv. Mater. 33 (2021), 2003741.
[4] Y. Zhao, X. Ren, Z. Xing, D. Zhu, W. Tian, C. Guan, Y. Yang, W. Qin, J. Wang, L. Zhang, Y. Huang, W. Wen, X. Li, R. Tai, In situ formation of hierarchical bismuth nanodots/graphene nanoarchitectures for ultrahigh-rate and durable potassium-ion storage, Small 16 (2020), 1905789.
[5] J.Y. Hwang, S.T. Myung, Y.K. Sun, Recent progress in rechargeable potassium batteries, Adv. Funct. Mater. 28 (2018), 1802938.
[6] Y. Wu, C. Zhang, H. Zhao, Y. Lei, Recent advances in ferromagnetic metal sulfides and selenides as anodes for sodium-and potassium-ion batteries, J. Mater. Chem. A 9 (2021) 9506–9534.
[7] Y. Hu, Y. Gao, L. Fan, Y. Zhang, B. Wang, Z. Qin, J. Zhou, B. Lu, Nitrogen doped intercalation TiO_2/TiN/$Ti_3C_2T_x$ nanocomposite electrodes with enhanced pseudocapacitance, Nanomaterials 10 (2020), 2002780.
[8] F. Yang, J. Hao, J. Long, S. Liu, T. Zheng, W. Lie, J. Chen, Z. Guo, Achieving high-performance metal phosphide anode for potassium ion batteries via concentrated electrolyte chemistry, Adv. Energy Mater. 11 (2021), 2003346.
[9] W. Zhang, J. Yin, W. Wang, Z. Bayhan, H. Alshareef, Status of rechargeable potassium batteries, Nano Energy 83 (2021), 105792.
[10] H. Wu, S.Y. Lu, S.Y. Xu, J. Zhao, Y.K. Wang, C. Huang, A. Abdelkader, W. Wang, K. Xi, Y. Guo, S.J. Ding, G.X. Gao, R.V. Kumar, Blowing iron chalcogenides into two-dimensional flaky hybrids with superior cyclability and rate capability for potassium-ion batteries, ACS Nano 15 (2021) 2506–2519.
[11] W. Zhang, Y. Liu, Z. Guo, Approaching high-performance potassium-ion batteries via advanced design strategies and engineering, Sci. Adv. 5 (2019) 7412.
[12] P. Xiong, J. Wu, M. Zhou, Y. Xu, Bismuth–antimony alloy nanoparticle@porous carbon nanosheet composite anode for high-performance potassium-ion batteries, ACS Nano 14 (2019) 1018–1026.
[13] R. Rajagopalan, Y. Tang, X. Ji, C. Jia, H. Wang, Advancements and challenges in potassium ion batteries: a comprehensive review, Adv. Funct. Mater. 30 (2020), 1909486.
[14] X. Min, J. Xiao, M. Fang, W. Wang, Y. Zhao, Y. Liu, A.M. Abdelkader, K. Xi, R. V. Kumar, Z. Huang, Potassium-ion batteries: outlook on present and future technologies, Energy Environ. Sci. 14 (2021) 2186–2243.
[15] J. Zheng, Y. Wu, Y. Sun, J. Rong, H. Li, L. Niu, Advanced anode materials of potassium ion batteries: from zero dimension to three dimensions, Nano-Micro Lett. 13 (2021) 1–37.
[16] X. Cheng, D. Li, Y. Wu, R. Xu, Y. Yu, Bismuth nanospheres embedded in three-dimensional (3D) porous graphene frameworks as high performance anodes for sodium-and potassium-ion batteries, J. Mater. Chem. A 7 (2019) 4913–4921.
[17] S. Imtiaz, I.S. Amiinu, Y. Xu, T. Kennedy, C. Blackman, K.M. Ryan, Progress and perspectives on alloying-type anode materials for advanced potassium-ion batteries, Mater. Today (2021), https://doi.org/10.1016/j.mattod.2021.02.008.
[18] K.-T. Chen, H.-Y. Tuan, Bi–Sb nanocrystals embedded in phosphorus as high-performance potassium ion battery electrodes, ACS Nano 14 (2020) 11648–11661.
[19] H. Gao, J. Niu, C. Zhang, Z. Peng, Z. Zhang, A dealloying synthetic strategy for nanoporous bismuth–antimony anodes for sodium ion batteries, ACS Nano 12 (2018) 3568–3577.
[20] Y. Zhao, A. Manthiram, High-capacity, high-rate bi–sb alloy anodes for lithium-ion and sodium-ion batteries, Chem. Mater. 27 (2015) 3096–3101.
[21] J. Wang, L. Fan, Z. Liu, S. Chen, Q. Zhang, L. Wang, H. Yang, X. Yu, B. Lu, In situ alloying strategy for exceptional potassium ion batteries, ACS Nano 13 (2019) 3703–3713.
[22] S. Guo, H. Li, Y. Lu, Z. Liu, X. Hu, Lattice softening enables highly reversible sodium storage in anti-pulverization Bi–Sb alloy/carbon nanofibers, Energy Storage Mater. 27 (2020) 270–278.
[23] L. Zhou, Z. Cao, W. Wahyudi, J. Zhang, J.-Y. Hwang, Y. Cheng, L. Wang, L. Cavallo, T. Anthopoulos, Y.-K. Sun, H.N. Alshareef, J. Ming, Electrolyte engineering enables high stability and capacity alloying anodes for sodium and potassium ion batteries, ACS Energy Lett. 5 (2020) 766–776.
[24] C. Zhang, H. Pan, L. Sun, F. Xu, Y. Ouyang, F. Rosei, Progress and perspectives of 2D materials as anodes for potassium-ion batteries, Energy Storage Mater. 38 (2021) 354–378.
[25] M. Lao, Y. Zhang, W. Luo, Q. Yan, W. Sun, S.X. Dou, Alloy-based anode materials toward advanced sodium-ion batteries, Adv. Mater. 29 (2017), 1700622.
[26] H. Wang, D. Zhai, F. Kang, Solid electrolyte interphase (SEI) in potassium ion batteries, Energy Environ. Sci. 13 (2020) 4583–4608.
[27] L. Vegard, Die konstitution der mischkristalle und die raumfüllung der atome, Z. Phys. 5 (1921) 17–26.
[28] Z. Wang, C. Duan, D. Wang, K. Dong, S. Luo, Y. Liu, Q. Wang, Y. Zhang, A. Hao, BiSb@ Bi_2O_3/SbO_x encapsulated in porous carbon as anode materials for sodium/potassium-ion batteries with a high pseudocapacitive contribution, J. Colloid Interface Sci. 580 (2020) 429–438.
[29] D. Li, J. Zhou, X. Chen, H. Song, Graphene-loaded Bi_2Se_3: a conversion–alloying-type anode material for ultrafast gravimetric and volumetric Na storage, ACS Appl. Mater. Interfaces 10 (2018) 30379–30387.
[30] K.-T. Chen, S. Chong, L. Yuan, Y.-C. Yang, H.-Y. Tuan, Conversion-alloying dual mechanism anode: nitrogen-doped carbon-coated Bi_2Se_3 wrapped with graphene for superior potassium-ion storage, Energy Storage Mater. 39 (2021) 239–249.
[31] S. Su, Q. Liu, J. Wang, L. Fan, R. Ma, S. Chen, X. Han, B. Lu, Control of SEI formation for stable potassium-ion battery anodes by Bi-MOF-derived nanocomposites, ACS Appl. Mater. Interfaces 11 (2019) 22474–22480.
[32] H. Liu, Z. Wang, Z. Wu, S. Zhang, S. Ge, P. Guo, M. Hua, X. Lu, S. Wang, J. Zhang, Direct tuning of meso-/micro-porous structure of carbon nanofibers confining Sb nanocrystals for advanced sodium and potassium storage, J. Alloy. Compd. 833 (2020), 155127.
[33] N. Cheng, J. Zhao, L. Fan, Z. Liu, S. Chen, H. Ding, X. Yu, Z. Liu, B. Lu, Sb-MOFs derived Sb nanoparticles@porous carbon for high performance potassium-ion batteries anode, Chem. Commun. 55 (2019) 12511–12514.
[34] Q. Tan, W. Zhao, K. Han, P. Li, W. Wang, D. He, Z. Liu, Q. Yu, M. Qin, X. Qu, The multi-yolk/shell structure of FeP@foam-like graphenic scaffolds: strong P–C bonds and electrolyte-and binder-optimization boost potassium storage, J. Mater. Chem. A 7 (2019) 15673–15682.
[35] B.F. Li, J. Zhao, Z.H. Zhang, C. Zhao, P.F. Sun, P.X. Bai, J.X. Yang, Z. Zhou, Y.H. Xu, Asymmetric distribution of cytokinins determines root hydrotropism in Arabidopsis thaliana, Cell Res. 29 (2019) 984–993.
[36] M. Gu, L. Fan, J. Zhou, A.M. Rao, B. Lu, Regulating solvent molecule coordination with KPF_6 for superstable graphite potassium anodes, ACS Nano 15 (2021) 9167–9175.
[37] Q. Liu, A.M. Rao, X. Han, B. Lu, Artificial SEI for superhigh-performance K-graphite anode, Adv. Sci. 8 (2021), 2003639.
[38] Z. Wang, K. Dong, D. Wang, S. Luo, Y. Liu, Q. Wang, Y. Zhang, A. Hao, C. Shi, N. Zhao, A nanosized SnSb alloy confined in N-Doped 3D Porous carbon coupled with ether-based electrolytes toward high-performance potassium-ion batteries, J. Mater. Chem. A 7 (2019) 14309–14318.
[39] J. Wu, Q. Zhang, S. Liu, J. Long, Z. Wu, W. Zhang, W.K. Pang, V. Sencadas, R. Song, W. Song, J. Mao, Z. Guo, Synergy of binders and electrolytes in enabling microsized alloy anodes for high performance potassium-ion batteries, Nano Energy 77 (2020), 105118.

[40] X. Wang, S. Zhang, Y. Shan, L. Chen, G. Gao, X. Zhu, B. Cao, X. He, In situ heterogeneous interface construction boosting fast ion/electron transfer for high-performances lithium/potassium storage, Energy Storage Mater. 37 (2021) 55–66.
[41] W. Zong, N. Chui, Z. Tian, Y. Li, C. Yang, D. Rao, W. Wang, J. Huang, J. Wang, F. Lai, T. Liu, Ultrafine MoP nanoparticle splotched nitrogen-doped carbon nanosheets enabling high-performance 3D-printed potassium-ion hybrid capacitors, Adv. Sci. 8 (2021), 2004142.
[42] H. Ding, J. Zhou, A.M. Rao, B. Lu, Cell-like-carbon-micro-spheres for robust potassium anode, Natl. Sci. Rev. (2020), nwaa276.
[43] Q. Zhang, X. Cheng, C. Wang, A.M. Rao, B. Lu, Sulfur-assisted large-scale synthesis of graphene microspheres for superior potassium-ion batteries, Energy Environ. Sci. 14 (2021) 965–974.
[44] S. Haghighat-Shishavan, M. Nazarian-Samani, M. Nazarian-Samani, K.-B. Kim, Electrolyte modulation of $BiPS_4$ concurrently suppressing the Bi coarsening and polysulfide shuttle effect in K-ion batteries, Energy Storage Mater. 39 (2021) 96–107.
[45] Z. Tian, N. Chui, R. Lian, Q. Yang, W. Wang, C. Yang, D. Rao, J. Huang, Y. Zhang, F. Lai, C. Liu, T. Liu, Dual anionic vacancies on carbon nanofiber threaded MoSSe arrays: a free-standing anode for high-performance potassium-ion storage, Energy Storage Mater. 27 (2020) 591–598.
[46] B. Wang, F. Yuan, Q. Yu, W. Li, H. Sun, L. Zhang, D. Zhang, Q. Wang, F. Lai, W. Wang, Amorphous carbon/graphite coupled polyhedral microframe with fast electronic channel and enhanced ion storage for potassium ion batteries, Energy Storage Mater. 38 (2021) 329–337.
[47] S. Zhang, Q. Fan, Y. Liu, S. Xi, X. Liu, Z. Wu, J. Hao, W.K. Pang, T. Zhou, Z. Guo, Dehydration-triggered ionic channel engineering in potassium niobate for Li/K-ion storage, Adv. Mater. 32 (2020), 2000380.
[48] H. Huang, J. Wang, X. Yang, R. Hu, J. Liu, L. Zhang, M. Zhu, Unveiling the advances of nanostructure design for alloy-type potassium-ion battery anodes via in situ TEM, Angew. Chem. 132 (2020) 14612–14618.
[49] K. Cao, H. Liu, Y. Jia, Z. Zhang, Y. Jiang, X. Liu, K.J. Huang, L. Jiao, Flexible antimony@ carbon integrated anode for high-performance potassium-ion battery, Adv. Mater. Technol. 5 (2020), 2000199.
[50] F. Ji, T. Liu, Y. Li, D. Li, L. Ci, Ball-milling strategy for fast and stable potassium-ion storage in antimony-carbon composite anodes, ChemElectroChem 7 (2020) 4587–4593.
[51] N. Zhao, J. Qin, L. Chu, L. Wang, D. Xu, X. Wang, H. Yang, J. Zhang, X. Li, Heterogeneous interface of Se@Sb@C boosting potassium storage, Nano Energy 78 (2020), 105345.
[52] H. Ding, J. Wang, L. Fan, Z. Liu, X. Jia, X. Yu, B. Lu, Sn-Sb compounds with novel structure for stable potassium storage, Chem. Eng. J. 395 (2020), 125147.
[53] S. Wang, P. Xiong, X. Guo, J. Zhang, X. Gao, F. Zhang, X. Tang, P.H. Notten, G. Wang, A stable conversion and alloying anode for potassium-ion batteries: a combined strategy of encapsulation and confinement, Adv. Funct. Mater. 30 (2020), 2001588.
[54] K. Li, X. Liu, Y. Qin, Z. Zhao, Y. Xu, Y. Yi, H. Guan, Y. Fu, P. Liu, D. Li, Sb_2S_3-Bi_2S_3 microrods with the combined action of carbon encapsulation and rGO confinement for improving high cycle stability in sodium/potassium storage, Chem. Eng. J. 414 (2021), 128787.
[55] T. Wang, D. Shen, H. Liu, H. Chen, Q. Liu, B. Lu, A Sb_2S_3 nanoflower/MXene composite as an anode for potassium-ion batteries, ACS Appl. Mater. Interfaces 12 (2020) 57907–57915.
[56] H. Liu, Y. He, K. Cao, S. Wang, Y. Jiang, X. Liu, K.J. Huang, Q.S. Jing, L. Jiao, Stimulating the reversibility of Sb_2S_3 anode for high-performance potassium-ion batteries, Small 17 (2021), 2008133.
[57] X. Zhang, Y. Rui, J. Yang, L. Wang, Y. Wang, J. Xu, Monodispersed SnO_2 microspheres aggregated by tunable building units as effective photoelectrodes in solar cells, Appl. Surf. Sci. 463 (2019) 679–685.
[58] X.-D. He, J.-Y. Liao, S. Wang, J.-R. Wang, Z.-H. Liu, X. Ding, Q. Hu, Z.-Y. Wen, C.-H. Chen, From nanomelting to nanobeads: nanostructured Sb_xBi_{1-x} alloys anchored in three-dimensional carbon frameworks as a high-performance anode for potassium-ion batteries, J. Mater. Chem. A 7 (2019) 27041–27047.
[59] J. Wang, B. Wang, B. Lu, Nature of novel 2D van der waals heterostructures for superior potassium ion batteries, Adv. Energy Mater. 10 (2020), 2000884.

Kuan-Ting Chen received her Ph.D. degree in Department of Chemical Engineering from National Tsing Hua University in Taiwan in 2021. Her research interests are in the areas of the synthesis and characterization of nanomaterials, and their applications in electrochemical energy storage such as lithium/potassium ion batteries.

Yi-Chun Yang received her M.S. degree at National Chiao Tung University in 2018. She is currently a research assistant in the Department of Chemical Engineering, National Tsing Hua University in Taiwan. Her research direction is the design and synthesis of nanomaterials for potassium ion batteries.

Lian-Ming, Lyu received the Ph.D. degree (2012) in Chemistry at National Tsing Hua University, Hsinchu, Taiwan. His current research interests in the energy conversion of nano-energy structural materials, focusing on the investigation and application of photochemical hydrogen production and electrochemical nitrogen fixation.

Ming-Yen Lu obtained his Ph.D. in 2009. He is currently an associate professor in Materials Science and Engineering at National Tsing Hua University, Taiwan. His research interests include characterization of low-dimensional materials, advanced TEM analysis, *in situ* dynamic study and the energy applications of materials.

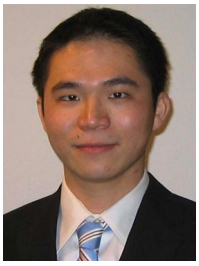

Hsing-Yu Tuan received his Ph.D. degree in Department of Chemical Engineering from the University of Texas at Austin in 2007. He is now a professor at National Tsing Hua University in Taiwan. His research focuses on nanomaterials synthesis and functionalization, and their applications in the fields of energy storage and conversion.